Research Article | Vol. 29, No. 11 / 24 May 2021 / Optics Express 16007

Optics EXPRESS

Freeform based hYperspectral imager for MOisture Sensing (FYMOS)

CHRISTOPHER GRAHAM,[1] JOHN M. GIRKIN,[1] AND CYRIL BOURGENOT[2,*]

[1] Department of Physics, Durham University, Durham DH1 3LE, UK
[2] Precision Optics Laboratory, Durham University, Sedgefield, TS21 3FB, UK
[*] cyril.bourgenot@durham.ac.uk

Abstract: We present FYMOS, an all-aluminum, robust, light weight, freeform based, near infrared hYperspectral imager for MOisture Sensing. FYMOS was designed and built to remotely measure moisture content using spectral features from 0.7-1.7µm integrating an InGaAs sensor. The imaging system, operating at F/2.8, is based on the three-concentric-mirror (Offner) spectrograph configuration providing a spectral resolution of 8 nm optimized for broad spectral coverage with sufficient resolution to make assessments of water levels. To optimize the optical performance, whilst minimizing weight and size, the design incorporates a bespoke freeform blazed grating machined on a commercial 5 axis ultra precision diamond machine. We achieve a 30% improvement on the RMS wavefront error in the spatial and spectral fields compared to a conventional Offner-Chrisp design with similar aperture and the monolithic Primary/Tertiary mirror eases the manufacturing assembly whilst minimizing weight. We demonstrate the performance of FYMOS by measuring the evaporation rate of water on a soil sample and results are processed with a physical multilayer radiative transfer model (MARMIT) to estimate the mean water thickness.

1. Introduction

Over the last two decades, hyperspectral imaging has become an essential tool in a wide variety of fields, from medical diagnoses, food quality assurance and mineral mapping. [1–3] One particular area where hyperspectral imagers have great potential, is in monitoring for precision agriculture enabling direct and remote acquisition of information on crop, soils, pests and weeds. Farmers are then able to respond to this information with locally optimized responses. Spatial distribution and temporal evolution of soil moisture are key parameters to monitor for water management optimisation. There are clear benefits in mapping and recording moisture during the growing season, in particular in arid areas, one of them being to efficiently irrigate the crop as, and when, required. Beyond precision irrigation, measurement of soil moisture variability between places and time of year helps to provide better understanding of (i) soil water retention capacity and erosion [4] (ii) drought forecasting and monitoring [5] (iii) as well as crop yield estimation and evapotranspiration rates [6,7].

A comprehensive study of the different technologies related to soil moisture measurements is given in [8]. Current methods involve either ground-based soil sensors, or remote sensing measurements on UAV or satellite platforms. The in-field techniques offer direct in-situ information, at a defined and controlled depth and provide the most accurate measurement. However, they do not allow for large scale surveys with high spatial or temporal resolution and additionally require a large number of operators. Flying sensing systems can make a difference since large swaths of farmland can be measured in a short period of time. Optically based sensing systems generally operate by comparing relative reflectance in different wavelength bands to

#425660 https://doi.org/10.1364/OE.425660
Journal © 2021 Received 23 Mar 2021; accepted 27 Apr 2021; published 10 May 2021

Optics EXPRESS

determine soil moisture content (SMC). A complete review of optical and thermal remote sensing instruments and methodology is given in [9]. One significant advantage of the "optical" range is the availability of the sun as a source for passive sensing. The sun's radiance, at the ground level, peaks in the visible with a broad spectral tail reaching 2400 nm, beyond which background thermal emissivity becomes predominant. The shortwave infrared range (SWIR, typically viewed as 0.9 to 1.7 μm) is interesting for SMC due to the large number of water absorption features and the sensitivity of the soil reflectance to moisture content in this wavelength range as well as the availability of a suitable source. However, due to the low penetration of light into soil, the measurements are limited to surface moisture measurements, but with prior knowledge of the dry soil surface reflectance, it is possible to recover the SMC using, physical or empirical models with various degrees of confidence depending on the soil type [10,11].

Passive sensing of moisture using solar light reflected from the soil does have to allow for the loss of some "excitation intensity" due to the absorption of light in the water bands during transmission through the atmosphere. In the InGaAs spectral sensitivity window SMC can been extracted using spectral indices, taking ratios of reflectance at wavelengths located at the edge of the water absorption bands [12,13], or based on radiative transfer models [6], [11], [14], [15]. One thus requires a SWIR hyperspectral imager with sufficient spectral resolution to separate the wavelengths bands of interest whilst maintaining both high signal levels and excellent spatial resolution.

Freeform optics (highly non-spherical shapes) have become an increasingly important tool for practical optical designs [16]. Freeforms are now found in all fields of optics, in the most advanced optical transmission devices [17,18], unobscured telescope designs for astronomical applications [19], free space communication using orbital angular momentum [20] and adjustable focus lenses based on Alvarez surfaces [21]. Their added value and high potential have also been demonstrated in mobile camera technologies [22]. With the recent development of new ultrafine aluminium alloys and progress in the field of directly machined freeform surfaces, diamond machined freeform reflective gratings offer a cost-effective, compact, and flexible alternative form of gratings. Their added value in potentially compact design make them promising components for space and UAV based hyperspectral imagers. Freeform gratings have been used so far in systems with low to medium spectral resolution [31][32].

This paper presents a compact, lightweight pushbroom hyperspectral imager called FYMOS (Freeform based hYperspectral imager for MOisture Sensing) which has been a purposely designed and manufactured with sufficiently high spectral and spatial resolution to monitor soil moisture specifically for drone-based platforms and optimised for InGaAs sensors. The FYMOS design, based on a F/2.8 Offner concept [23] utilizes a bespoke freeform diffraction grating which as well as providing optical "power" contains a component of asymmetry to correct and compensate for the inherently asymmetry in the beam path during dispersion by the grating, offering a pixel limited performance in the [0.7-1.7 μm] band.

2. Instrument

2.1. Design concept

Offner type spectrograph designs have already been studied in detail and can be identified in the following families:

- All spherical surfaces, with identical M1/M3 concentric with the grating [24]
- Spherical Offner-Chrisp design, where the primary and tertiary mirrors have different radii of curvature, but remain concentric with the spherical grating [25]
- Freeform Offner–Chrisp compact design [23]

Optics EXPRESS

The FYMOS design is a simplified variation of the freeform Offner type, where the primary and tertiary mirrors are the same spherical surface (to simplify manufacturing), with the addition of a freeform grating. The design, based on parameters presented in Table 1, was driven by two constraints : (i) the grating period (10 microns) that can be comfortably machined by 4 axis ruling with the diamond V-shape tool (ii) the requirement to cover at least a 6 x 4 mm sensor over the VIS/NIR extended spectral range [0.7-1.7 microns] of InGaAs sensors [26] where the InP substrate is thinned out to extend the sensitivity range toward the short wavelength. To cover the full dimensions of the sensor we consider the dispersion along the small axis (4 mm) and the slit along the long axis (6 mm) and the spectral linear dispersion at the image plan, ζ at 250 nm/mm. The grating density, l, is 100 mm^{-1}. The radius of curvature R_g of the convex grating is given by [23] :

$$R_g = \frac{1}{ml\zeta}$$

and calculated to be 40mm at diffraction order $m = 1$.

Table 1. Spectrograph parameters serving as a basis in the optimization.

F/#	2.8
Wavelength	[0.7-1.7μm]
Slit Size	6 mm
Sensor Size	6x4 mm

The broken symmetry caused by the diffraction grating in an Offner imaging spectrometer, where the primary and tertiary mirrors are identical, induces aberrations. Chrisp proposed a design where this asymmetry was partly compensated by separating the primary/tertiary mirror into two unique spherical entities with different radii of curvature, whilst keeping the constraint on the concentricity.

In the FYMOS design, the primary/tertiary mirror is kept as a single spherical entity and the partial compensation of the dispersive asymmetry is achieved by giving the grating a freeform shape. The freeform optimization was performed by adding two XY polynomial terms to a spherical shape with a base radius of 40 mm: (i) X0Y1, which is a tilt term around the axis normal to the propagation plane and (ii) X2Y1, which is an astigmatic term with a quadratic profile also along the axis normal to to the propagation plane. Only XY polynomial terms were available for the optimization. They are not orthogonal, so their contribution does not add up independently.

The optimization in Zemax ray tracing software was performed using 9 field sampling points (3 spatial [-3,0,3 mm] and 3 spectral points [0.7, 1.2, 1.7micron]) with equal optimization weight, while minimizing the RMS wavefront error (with Piston and Tip/tilt removed).

To identify the gain in performance specifically brought by the FYMOS freeform grating design compared to other types of Offner-based spectrograph designs, 4 cases were modeled. The layouts are shown in Fig. 1:

a). An all-spherical design, where the primary/tertiary have the same radius of curvature and are concentric with secondary (spherical grating).

b). A similar design to item (a), but whose RMS spot sizes were optimized by tilting the grating around the x axis.

c). An all spherical Offner-Chrisp design, with a primary and tertiary mirror with different radii of curvature and concentric centres of curvature.

Optics EXPRESS

d). A similar design to items (a) and (b) but optimized with a freeform grating.

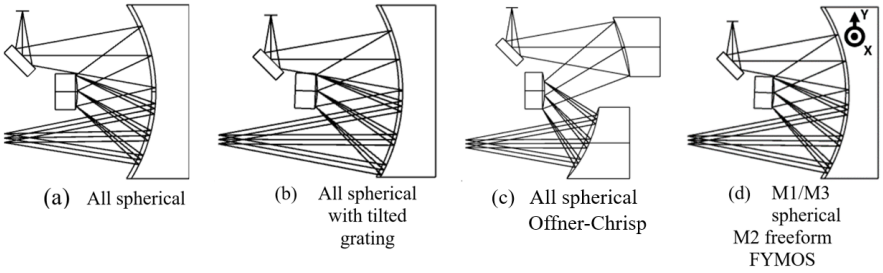

Fig. 1. Design comparison of 4 optimization cases. (a) is an all-spherical design, which is, in essence, an Offner relay with a spherical grating. (b) is similar to (a) but with a tilted spherical grating. (c) is an Offner-chrisp design where the primary and tertiary mirrors have different radii of curvature. (d) is the design use for FYMOS, which is similar to (b) but with a X0Y1 and X2Y1 polynomial terms added to the spherical grating. The grating lines are along the Y axis.

Figure 2 compares the performance in terms of the RMS Wavefront Error (WFE) averaged over the spatial and spectral fields. For the all-spherical design in case (a), Astigmatism remains the main contributor to the WFE. The all-spherical performance is used as a baseline comparison for the 3 other configurations. In case (b), tilting the grating during the optimization leads to an improvement in the WFE of around 30% with an aberration transfer from Astigmatism to Trefoil. The Offner-Chrisp design in case (c) offers the same level of Astigmatism as case (b), but with around 3 times less Trefoil. Case (d) shows that the freeform shape balancing both Trefoil and Astigmatism with a 3-fold improvement with respect to the all-spherical baseline design.

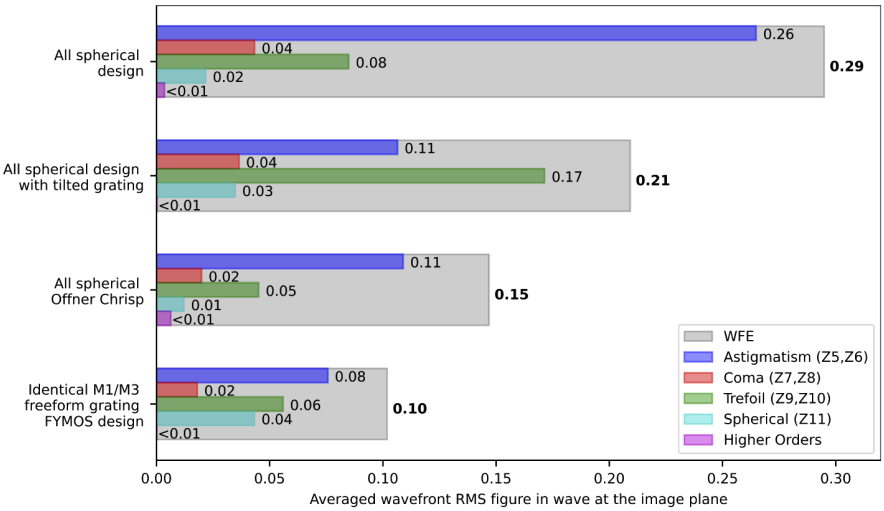

Fig. 2. Bar chart showing the average wavefront RMS figure in the spatial and spectral fields (grey bars), with a breakdown of the first 11 standard Zernike terms, plus the higher orders (magenta). The Zernike terms add up in RMS to produce the average wavefront RMS.

The FYMOS design was assessed in terms of the spot size RMS (Fig. 3(a)) in the full spatial and spectral field and image distortion (Fig. 3(b)) achieving less than 10 microns of "smile".

Optics EXPRESS

Figure 3(c) shows the mapped freeform shape with best fit sphere removed. The freeform residual is equivalent to 6 microns over the 16 mm diameter of the aperture. It was subsequently measured in the Littrow configuration using a phase shifting interferometer (Fig. 3(d)). The groove profile was optimized for a blaze wavelength of 1 micron (corresponding to a blaze angle of 2.8°), diffraction order 1, a line density of 100 lines/mm and an incidence angle of 25.5°. The grating delivers maximal efficiency in the [0.7-1.7] microns range. The groove profile and period were checked on a white light interferometer (Fig. 3(e)). At least 4 axis were needed for the machining of freeform gratings: 3 linear axes (X, Y and Z) to follow the shape of the freeform substrate, and an additional angular axis (B) to enable the rotation of the diamond tool cutting edge and to produce a constant blaze angle on a curved surface. The grating was produced in house on a 5 axis Moore Nanotech Freeform Generator machine.

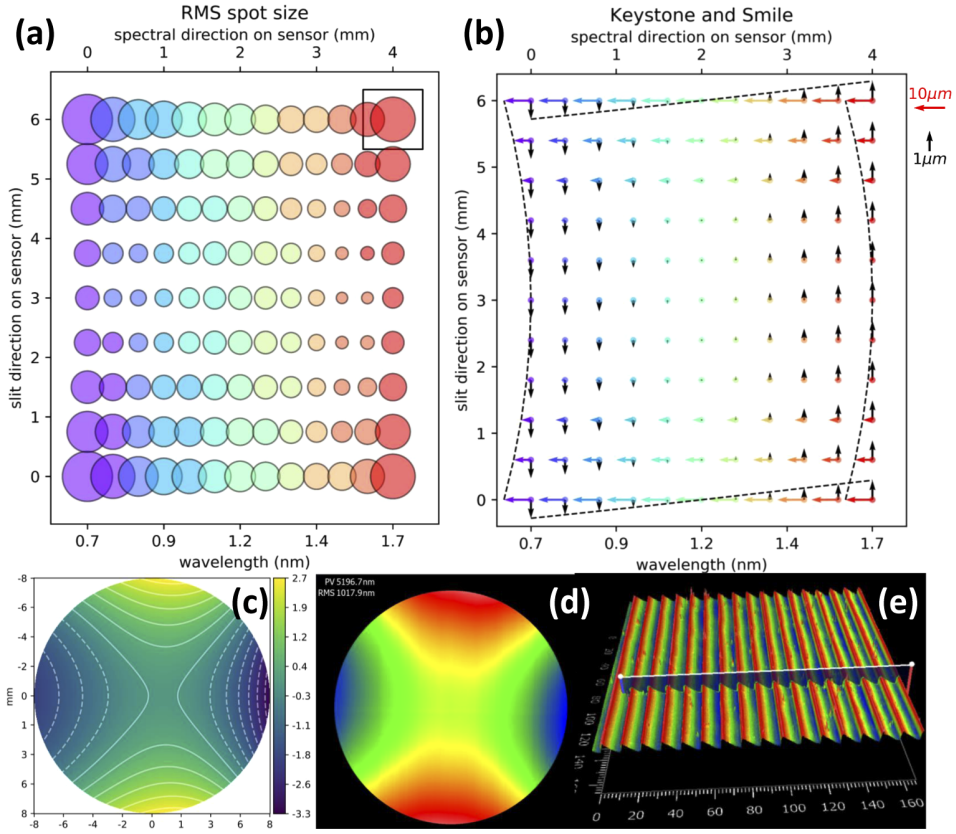

Fig. 3. (a) RMS Spot size in the field. The square is of size 10 x 10 microns for comparison. (b), the distortion Smile and Keystone are computed to be respectively less than 10 microns and 1 micron (c) Surface Sag at the best fit sphere (40mm) showing the amplitude of the freeform surface correction needed. The colorbar is in microns. (d) Surface form deviation measured in the Littrow configuration at best tip, tilt and sphere, measured with a Zygo Verifire phase shifting interferometer. (e) Groove profile measured with a whitelight interferometer Zygo Zegage Plus equipped with an objective x20.

A diagram of the system is shown in Fig. 4(a) and 4(b), with the light rays propagating from top to bottom. Light is focused onto the entrance of an adjustable slit (Thorlabs VA100C/M) by the front lens (Kowa LM25HC-SW F/1.4, a SWIR coated lens with a focal length of 25mm), before being reflected by the fold mirror onto the primary/tertiary mirror. The light is then

Optics EXPRESS

reflected onto the freeform diffraction grating, with the dispersed beam being focused by the primary/tertiary mirror onto the camera sensor.

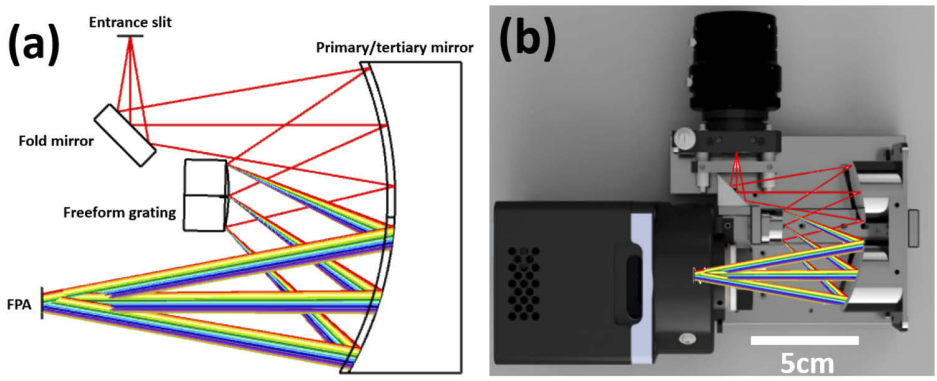

Fig. 4. (a) Optical Diagram of the FYMOS spectrograph, (b) render of mechanical design inset.

The focal plane array (FPA) is a SWIR Snake InGaAs camera (Photonic Science, Saint Leonards-on-sea, UK). The sensor has a pixel count of 640 x 512, with a spectral response from [900-1700 nm] and utilizes a GigE interface and inbuilt cooling system.

FYMOS is a pushbroom hyperspectral imager, with 640 pixels allocated to the spatial direction and 512 pixels to the spectral direction. When used in the laboratory the motion required for pushbroom scanning is enabled with a computer-controlled rotation stage (Standa, Lithuania). The motor and camera controllers are synced together using a laptop running a home written python program. Both the spatial and spectral resolutions are limited by the pixel size: 15 microns. The spectral resolution is 8 nm.

3. Spectral calibration

The spectral calibration of the instrument was carried out using a computer-controlled Omni-lambda 300 monochromator, using a temperature regulated tungsten halogen lamp as the illumination source. The monochromator was scanned from 1000 nm to 1700 nm, with the location of the center of the peak recorded every 20 nm. These values were used to generate a look up table of sensor pixel number to wavelength. From this, the mean dispersion per spectral pixel was found to be 4 nm. A set of infrared bandpass filters were then used to verify the calibration, with the measured peaks of the filters matching the expected wavelength value within 4nm, or 1 spectral pixel.

A simple computer model was created to calculate the effective sensitivity of the system across the usable wavelength range. This model includes the wavelength dependent effects of lens transmission, diffraction grating efficiency and detector quantum efficiency. Including the spectral power distribution of the tungsten halogen lamp provided by the manufacturer [27], a comparison between the model and the real instrument can be made and is shown in Fig. 5. The data for the model has been interpolated from mean manufacturer's data for each component. The error fill area for the model and the error bars on the filters were calculated by considering the errors introduced by the manufacturing tolerances of each component and propagating them through the model. The overall shape of the modelled spectrum matches well with the measured lamp spectrum, providing confidence that the system is functioning as intended.

Optics EXPRESS

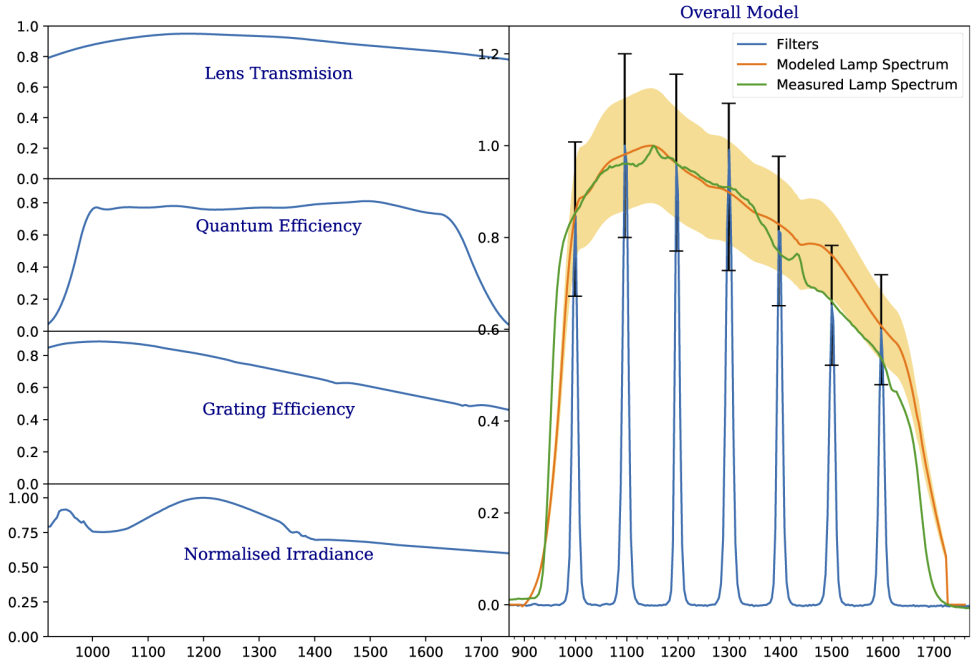

Fig. 5. Spectral calibration of FYMOS, using a set of narrow bandpass filters (10nm FWHM). The left plots show the effect on the spectrum of the various contribution along the beam path from the lens transmission (top), the quantum efficiency of the InGaAs sensor, the diffraction grating efficiency modelled with the scalar diffraction theory and the tungsten lamp irradiance at 2796K [27]

4. Results

4.1. Water on soil evaporation

The experimental setup is shown in Fig. 6 with the sample being illuminated with a 70 watt thermally regulated tungsten halogen lamp. In order to test the instrument, a local clay rich soil sample was collected and initially dried on a hot plate. After cooling, 3.5 grams of water were added to the surface of the soil sample and allowed to soak in. The heating plate was then activated to a temperature of 60 °C. As the water evaporated, a datacube was recorded every 90 seconds for 40 minutes, until the soil had completely dried out. A reference hyperspectral image of a 99% reflectance Zenith panel was captured under the same conditions to enable conversion from radiance to reflectance maps.

An example of a reflectance map is shown in Fig. 7(a). This map shows the measured reflectance of the soil and water at 1400 nm, a wavelength in which water absorption of IR light is particularly strong. The dry soil has a reflectance of close to 15%, whereas the saturated soil has a reflectance of 5%. The mean reflectance over 100 spatial pixels in a 10 x 10 pixel square was calculated for each time step, shown in Fig. 7(b). As the soil dries out, its reflectance increases across the entirety of the measured spectrum. Notably, the dip centered at 1440 nm seen in the wet soil becomes less pronounced as the soil dries.

4.2. Moisture content

There are multiple techniques for recovering soil moisture from reflectance measurements ranging from normalized difference indices, which compare reflectance measured between two or more

Optics EXPRESS

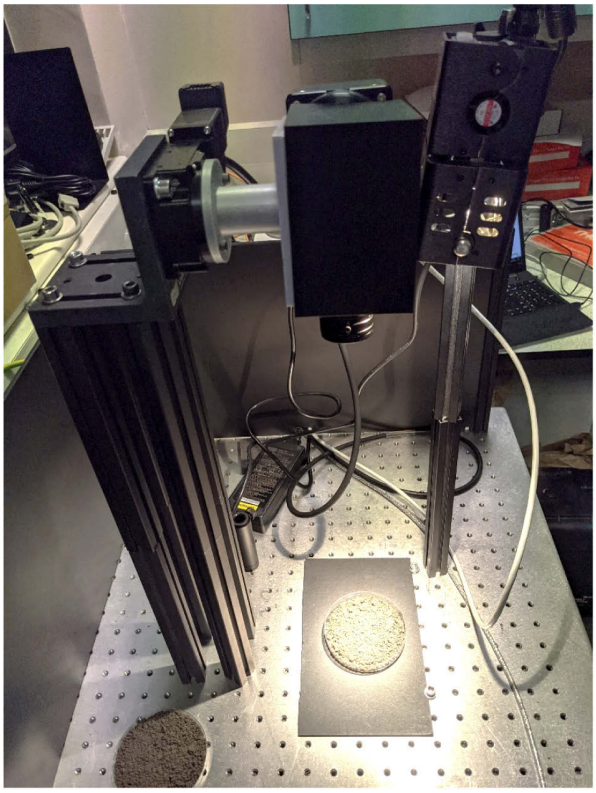

Fig. 6. Experimental setup of FYMOS for capturing hyperspectral images of soil. The light source is mounted as close to on axis as possible to minimize illumination gradients.

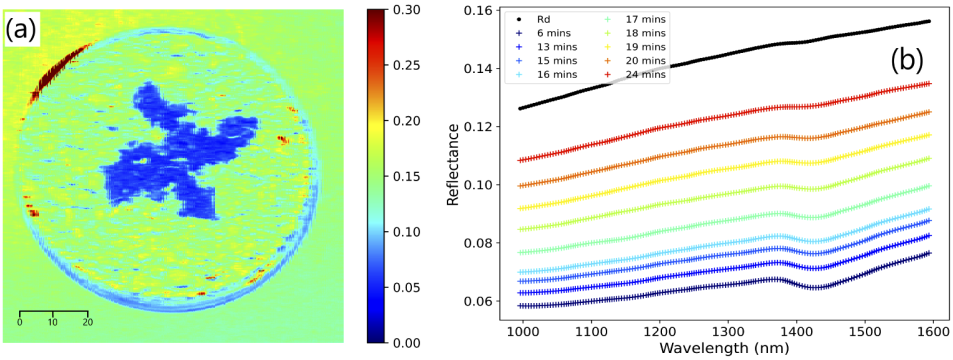

Fig. 7. (a) Reflectance map of mixed wet and dry soil sample taken at 1440 nm. Image scale is in mm. This wavelength is at a peak in the IR water absorption spectrum, giving a strong contrast. The reflectance of the wet soil is close to 5% at this wavelength, while the dry soil has a reflectance of 15%. (b) Mean reflectance over a 5x5mm area of damp soil as it dries. As the soil dries, the reflectance increases across the spectrum. The dip centered around 1440 nm visible in the wet soil becomes less pronounced as it dries.

Optics EXPRESS

wavelength bands, to general shape methods [6]. As we wish to use the final instrument outside the laboratory, we used a method based upon line fitting to the physical radiative transfer model called MARMIT [11]. MARMIT builds on the models proposed by Angström and later Bach. This model predicts the reflectance of a wet soil by characterizing it as a dry soil covered by a thin layer of water. By fitting the MARMIT model to a measured reflectance spectrum using a reference dry spectrum, the SMC can then be estimated. The fit of the model is determined by two parameters, the water depth, and the fraction of the surface covered by water. Multiplying these together gives a measure of the mean water thickness. SMC can then be retrieved from the mean water thickness through an assessment step which uses a reference dataset where the relation between SMC and mean water thickness has been calibrated beforehand. Figure 8 shows the model being applied to the drying soil's measured reflectance, with the dotted line being the mean measured reflectance over 100 pixels, and the continuous line showing the model's output. The fit between the modeled and measured reflectances is in excellent agreement, with R2 values above 0.99 for all time steps.

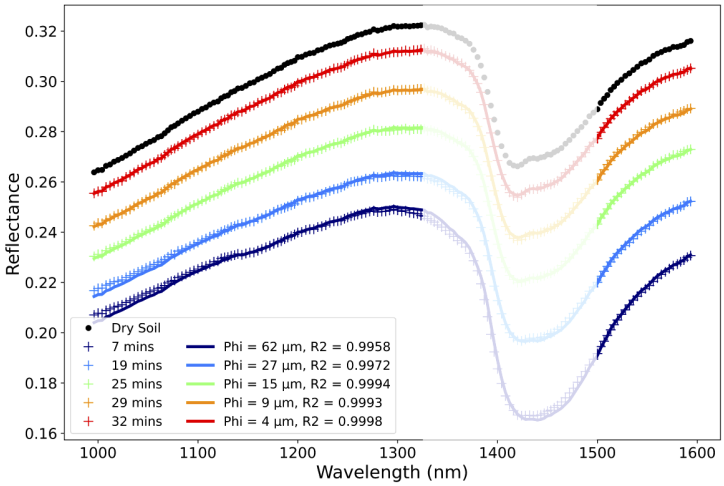

Fig. 8. MARMIT model applied to drying clay rich soil, excluding the 1400nm atmospheric absorption band. The measured reflectance values are plotted as crosses, while the model is plotted as a solid line. While the soil has a differently shaped spectrum compared to the first sample, the changes to the spectrum as the soil dries are similar.

Under real field conditions and passive illumination of the soil by the sun, the 1400 nm region of the spectrum will be unavailable due to the strong atmospheric absorption in this band. To simulate this, the data in this region of the spectrum was excluded when calculating the fit. The unavailability of light in this wavelength range also prevents imaging of the soil at the wavelengths where the contrast between wetter and drier soil is highest. Instead, a map of the mean water depth can be created to visualize the distribution of water content in the sample. To illustrate this, a patch of soil was artificially moisturized following the outline of Durham University's shield logo as shown in Fig. 9(c). Both the image taken at 1400 nm (Fig. 9(a)) and the mean water thickness computed on a range excluding the 1340-1500nm band (Fig. 9(b) can be compared. The shape of the calculated map fits well with both the visible and infrared images. A timelapse of the calculated map changing with time can be seen in Visualization 1. Areas where the fit failed were left at value 0.

Shown in Fig. 9(d), the value of the mean water depth estimated by the model, decreases monotonically with time as the water content evaporates.

Optics EXPRESS

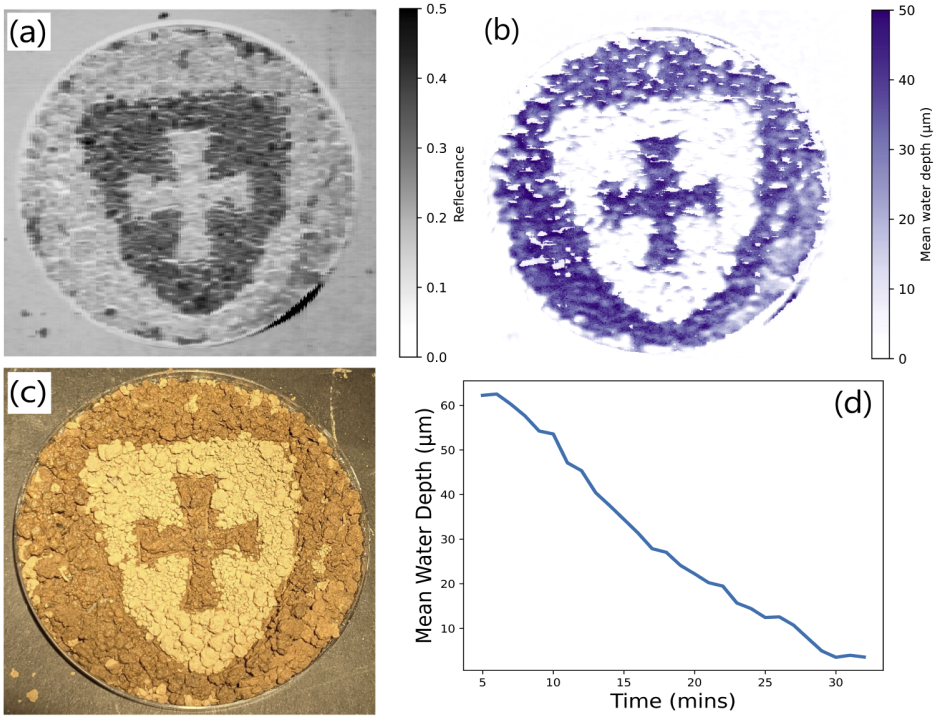

Fig. 9. (a) Reflectance map of mixed wet and dry soil sample taken at 1440 nm.(b) Map of mean water depth (in micron), calculated excluding 1400 nm atmospheric absorption band. Under ground level solar illumination, the 1440 nm band would be unavailable due to atmospheric absorption. The use of these parameters emulates spatial mapping of soil moisture close to outdoor conditions. See Visualization 1. (c) Image of damp soil taken with a smartphone camera. The petri dish has a diameter of 90 mm. (d) Mean water depth value calculated from MARMIT model decreasing monotonically with time. This was calculated as a mean of 100 spatial pixels in a 10x10 pixel square. This value can be subsequently link to the amount of water present on the soil surface.

This model was developed using laboratory measurements under controlled illumination, with few in-field measurements being available. These in-field measurements are important in determining how successfully the model can be applied in real world conditions (on heterogeneous soil with possible presence of biomass), using solar illumination instead of controlled lighting. The next step for this instrument will be to deploy it on a drone to collect in-field measurements.

5. Conclusion

In conclusion, the design, manufacture, calibration and first experiments of a compact hyperspectral imager called FYMOS, have been presented. The imaging system makes use of a freeform blazed diffraction grating to achieve as 30% reduction in RMS wavefront error in both spatial and spectral fields compared to a conventional Offner-Chrisp design using a similar aperture. Operating over a wavelength range of [1000-1700 nm] (but designed for covering 700- 1700nm]) with a spectral resolution of 8 nm, the instrument has been optimized for remote measurement of soil moisture levels using reflectance spectra on a temperature controlled InGaAs sensor.

Optics EXPRESS

After calibration, FYMOS was used in a lab to take reflectance measurements of a drying soil sample, with the results fitted with the physical radiative transfer model MARMIT to display and monitor real time moisture content variation induced by natural evaporation.

Funding. Engineering and Physical Sciences Research Council (EP/S001727/1).

Acknowledgments. This work was supported by an UKRI- EPSRC Innovation fellowship "A compact novel hyperspectral imager for more reliable and precise agriculture".

Disclosures. The authors declare no conflicts of interest.

Data availability. Data underlying the results presented in this paper are not publicly available at this time but may be obtained from the authors upon reasonable request.

References

1. G. Lu and B. Fei, "Medical hyperspectral imaging: a review," J. Biomed. Opt. **19**(1), 010901 (2014).
2. C. Zhang, C. Guo, F. Liu, W. Kong, Y. He, and B. Lou, "Hyperspectral imaging analysis for ripeness evaluation of strawberry with support vector machine," J. Food Eng. **179**, 11–18 (2016).
3. R. Jain and R. U. Sharma, "Airborne hyperspectral data for mineral mapping in Southeastern Rajasthan, India," International Journal of Applied Earth Observation and Geoinformation **81**, 137–145 (2019).
4. F. M. Ziadat and A. Y. Taimeh, "Effect of rainfall intensity, slope, land use and antecedent soil moisture on soil erosion in an arid environment," Land Degrad. Develop. **24**(6), 582–590 (2013).
5. B. R. Parida, W. B. Collado, R. Borah, M. K. Hazarika, and L. Samarakoon, "Detecting drought-prone areas of rice agriculture using a MODIS-derived soil moisture index," GIScience and Remote Sensing **45**(1), 109–129 (2008).
6. J. Yuan, X. Wang, C. X. Yan, S. R. Wang, X. P. Ju, and Y. Li, "Soil moisture retrieval model for remote sensing using reflected hyperspectral information," Remote Sens. **11**(3), 366 (2019).
7. W. W. Verstraeten, F. Veroustraete, and J. Feyen, "Assessment of evapotranspiration and soil moisture content across different scales of observation," Sensors **8**(1), 70–117 (2008).
8. S. U. Susha Lekshmi, D. N. Singh, and M. Shojaei Baghini, "A critical review of soil moisture measurement," Measurement: Journal of the International Measurement Confederation **54**, 92–105 (2014).
9. D. Zhang and G. Zhou, "Estimation of soil moisture from optical and thermal remote sensing: A review," Sensors **16**(8), 1308 (2016).
10. M. L. Whiting, L. Li, and S. L. Ustin, "Predicting water content using Gaussian model on soil spectra," Remote Sensing of Environment **89**(4), 535–552 (2004).
11. A. Bablet, P. V. Vu, S. Jacquemoud, F. Viallefont-Robinet, S. Fabre, X. Briottet, M. Sadeghi, M. L. Whiting, F. Baret, and J. Tian, "MARMIT: A multilayer radiative transfer model of soil reflectance to estimate surface soil moisture content in the solar domain (400 - 2500 nm)," Remote Sensing of Environment **217**, 1–17 (2018).
12. S. Fabre, X. Briottet, and A. Lesaignoux, "Estimation of soil moisture content from the spectral reflectance of bare soils in the 0.4–2.5 μm domain," Sensors **15**(2), 3262–3281 (2015).
13. Y. Zhang, K. Tan, X. Wang, and Y. Chen, "Retrieval of Soil Moisture Content Based on a Modified Hapke Photometric Model: A Novel Method Applied to Laboratory Hyperspectral and Sentinel-2 MSI Data," Remote Sens. **12**(14), 2239 (2020).
14. H. Bach and W. Mauser, "Modelling and model verification of the spectral reflectance of soils under varying moisture conditions," Int. Geosci. Remote. Sens. Symp. (IGARSS) **4**, 2354–2356 (1994).
15. M. Sadeghi, S. B. Jones, and W. D. Philpot, "A linear physically-based model for remote sensing of soil moisture using short wave infrared bands," Remote Sensing of Environment **164**, 66–76 (2015).
16. K. P. Thompson and J. P. Rolland, "Freeform Optical Surfaces: A Revolution in Imaging Optical Design," Opt. Photonics News **23**(6), 30 (2012).
17. D. Cheng, Y. Wang, H. Hua, and M. M. Talha, "Design of an optical see-through head-mounted display with a low f-number and large field of view using a freeform prism," Appl. Opt. **48**(14), 2655 (2009).
18. R. R. Boye, W. C. Sweatt, B. H. Jared, A. M. Ison, E. G. Winrow, M. P. Saavedra, and J. P. Hunt, "Design of head-mounted binoculars utilizing freeform surfaces," Opt. Eng. **53**(3), 031310 (2013).
19. K. Fuerschbach, J. P. Rolland, and K. P. Thompson, "A new family of optical systems employing ϕ-polynomial surfaces," Opt. Express **19**(22), 21919 (2011).
20. M. P. J. Lavery, D. J. Robertson, G. C. G. Berkhout, G. D. Love, M. J. Padgett, and J. Courtial, "Refractive elements for the measurement of the orbital angular momentum of a single photon," Opt. Express **20**(3), 2110 (2012).
21. S. Barbero and J. Rubinstein, "Adjustable-focus lenses based on the Alvarez principle," J. Opt. **13**(12), 125705 (2011).
22. F. Duerr, Y. Meuret, and H. Thienpont, "Potential benefits of free-form optics in on-axis imaging applications with high aspect ratio," Opt. Express **21**(25), 31072 (2013).
23. J. Reimers, A. Bauer, K. P. Thompson, and J. P. Rolland, "Freeform spectrometer enabling increased compactness," Light: Sci. Appl. **6**(7), e17026 (2017).
24. D. Kwo, G. Lawrence, and M. Chrisp, "Design Of A Grating Spectrometer From A 1:1 Offner Mirror System," in *Current Developments in Optical Engineering II*, vol. 0818 R. E. Fischer and W. J. Smith, eds., International Society for Optics and Photonics (SPIE, 1987), pp. 275–281.

Optics EXPRESS

25. X. Prieto-Blanco, C. Montero-Orille, B. Couce, and R. de la Fuente, "Analytical design of an Offner imaging spectrometer," Opt. Express **14**(20), 9156 (2006).
26. S. Manda, R. Matsumoto, S. Saito, S. Maruyama, H. Minari, T. Hirano, T. Takachi, N. Fujii, Y. Yamamoto, Y. Zaizen, T. Hirano, and H. Iwamoto, "High-definition visible-swir ingaas image sensor using cu-cu bonding of iii-v to silicon wafer," in *2019 IEEE International Electron Devices Meeting (IEDM)*, (2019), pp. 16.7.1–16.7.4.
27. Thorlabs, "SLS201 Spectral Power Distribution,".